Steel and Composite Structures, *Vol. 20, No. 3 (2016) 693-718*
DOI: http://dx.doi.org/10.12989/scs.2016.20.3.693

Iterative global-local procedure for the analysis of thin-walled composite laminates

Ashkan Afnani [a] and R. Emre Erkmen*

School of Civil and Environmental Engineering, University of Technology Sydney, NSW 2007, Australia

(*Received March 17, 2015, Revised October 20, 2015, Accepted December 03, 2015*)

Abstract. This paper presents a finite element procedure based on Bridging multi-scale method (BMM) in order to incorporate the effect of local/cross-sectional deformations (e.g., flange local buckling and web crippling) on the global behaviour of thin-walled members made of fibre-reinforced polymer composite laminates. This method allows the application of local shell elements in critical regions of an existing beam-type model. Therefore, it obviates the need for using computationally expensive shell elements in the whole domain of the structure, which is otherwise necessary to capture the effect of the localized behaviour. Consequently, highly accurate analysis results can be achieved with this method by using significantly smaller finite element model, compared to the existing methods. The proposed method can be used for composite polymer laminates with arbitrary fibre orientation directions in different layers of the material, and under various loading conditions. Comparison with full shell-type finite element analysis results are made in order to illustrate the efficiency and accuracy of the proposed technique.

Keywords: iterative global-local analysis; bridging multi-scale method; buckling; composite members; local deformations

1. Introduction

The use of fibre-reinforced polymer composite laminated plates as a construction material has increased in recent years. The primary reason for this increase is their non-corrosive nature and long term durability, high tensile strength-to-weight ratio, electromagnetic neutrality and resistance to chemical attack. Because of their high strength-to-weight ratios, slender structural components may be formed by using composite laminates, which can be used in building, bridge, aerospace and marine applications. These structural materials are often cast in beam-type shapes (i.e., large span in comparison to cross-sectional dimensions), for which they are commonly analysed by using beam type elements. A beam formulation was developed by Bauld and Tzeng (1984), which can capture flexural and lateral-torsional buckling behaviour of thin-walled composite laminated members. Closed form analytical solutions for buckling analysis based on beam-type formulations can be found in the studies of Pandey *et al*. (1995), Kollár (1991), Sapkás amd Kollár (2002), Kim *et al*. (2007), Roberts (2002) and Roberts and Masri (2003), which are limited to certain boundary and loading conditions. On the other hand, the finite element method can be used to obtain

*Corresponding author, Ph.D., Lecturer, E-mail: emre.erkmen@uts.edu.au
[a] Graduate Research Assistant, E-mail: ashkan.afnaniesfandabadi@student.uts.edu.au

http://www.techno-press.org/?journal=scs&subpage=6 ISSN: 1229-9367 (Print), 1598-6233 (Online)

solutions that are applicable to general boundary conditions and loading cases. For the flexural-torsional buckling analysis of thin-walled composite beams, finite element formulations were developed by Omidvar and Ghorbanpoor (1996), Lee *et al*. (2002), Lee (2006), Back and Will (2008) and Cardoso *et al*. (2009). These types of elements are formulated based on the assumption that cross-sections remain rigid during the deformation, which limits their application to axis-related deformations only (i.e., flexural, torsional and flexural-torsional buckling), and hence they cannot capture local/cross-sectional deformations such as flange local buckling and web crippling. If the effect of the local deformations is needed to be considered, shell-type elements have to be adopted.

On the other hand, the focus of the recent research in numerical methods has been on adaptive numerical strategies such as meshfree methods, e.g., (Belytschko *et al*. 1996, Erkmen and Bradford 2011, Liu *et al*. 1997, Oden *et al*. 2006), generalised finite element methods, e.g., (Belytschko *et al*. 2001, Strouboulis *et al*. 2001), multi-scale methods, e.g., (Feyel 2003, Fish *et al*. 1994, Geers *et al*. 2010, Hughes *et al*. 1998, Hughes and Sangalli 2007, Liu *et al*. 2000) and the use partition of unity concept (Babuška *et al*. 2003, Babuška and Melenk 1997, Li and Liu 2002, Schafer 2008). These methods allow accuracy improvements only at desired locations without necessitating changes in the global numerical model of the structure, especially; the partition of unity concept has been used for overlapping decomposition in the analysis domain in order to achieve enrichment in local deformation fields. Similarly, the Bridging Multiscale Method (BMM) provides a mathematical basis for the analysis of physical phenomena that are coupled based on two different level of physical assumption, e.g., (Kadowaki and Liu 2004) by splitting the simple/global analysis domain from the local/sophisticated modelling. Consequently, it can be utilized to split the analysis domain based on the level of desired accuracy.

In thin-walled members, the interaction of local and global deformation modes can give rise to multiple scales in the deformation fields (Bradford and Hancock 1984). In order to capture local buckling behaviour, specialised finite strip formulations, e.g., (Bradford 1992), generalised beam theory, e.g., (Davies *et al*. 1994), and shell-type elements, e.g., (Ronagh and Bradford 1996) have been utilised. Recently, Erkmen (2013) has developed a numerical technique based on the BMM that incorporates the effects of local deformations in the overall behaviour of thin-walled structural members. This approach allows for the employment of two kinematic models in the numerical analysis. While simple beam-type elements are used for the analysis of the overall structure, more sophisticated shell-type elements are employed for the local fine-scale analysis in a relatively narrow span of the member. In the present, the application of the method is expanded for composite thin-walled members. Comparisons with full shell and beam-type models are provided in order to illustrate the efficiency of the analysis proposed in the present paper.

The paper is organised as follows: the kinematics and the weak form of the equilibrium equations for both beam-type and shell-type analyses are given briefly. Following this, the proposed iterative global-local analysis procedure is introduced in detail. Numerical examples are then presented, and conclusions are drawn in the final section.

2. Beam-type analysis

2.1 Kinematic assumptions

In order to simplify the global analysis, a thin-walled beam formulation is used, which is based on second-order nonlinear thin-walled beam theory (Trahair 2003). For this: (a) each segment of

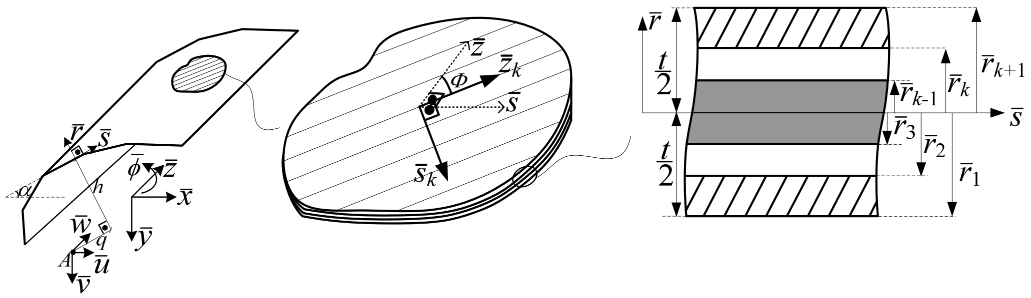

(a) Thin-walled beam (b) Fibre orientations (c) Laminates across the thickness

Fig. 1 Thin-walled beam composed of fibre-reinforced laminates

the cross-section behaves as a Kirchhoff plate with additional membrane behaviour; (b) the contour of the cross-section does not deform in its plane; and (c) normal stresses within the cross-sectional plane vanish. These assumptions imply that the nonzero strains in the thin-walled beam strain vector $\bar{\varepsilon}$ result from the axial strains induced by membrane, bending and torsional actions (bimoment), as well as from shear strains induced by uniform torsion. The strain components can be written in terms of deflections $\bar{u}(\bar{z})$, $\bar{v}(\bar{z})$ and $\bar{w}(\bar{z})$ which are parallel to $\bar{x}$, $\bar{y}$ and $\bar{z}$ directions respectively, and the angle of twist $\bar{\phi}$ of the cross-section (Fig. 1(a)) as given in Appendix A. The finite element formulation is developed by using linear interpolation for $\bar{w}$ and cubic interpolations for $\bar{u}$, $\bar{v}$ and $\bar{\phi}$. The displacement of a point on the cross-section $\bar{\mathbf{u}}$ can be written in terms of the vector of nodal displacements $\bar{\mathbf{d}}$ as $\bar{\mathbf{u}} = \mathbf{N}\bar{\mathbf{d}}$. Explicit expression for $\bar{\mathbf{u}}$, $\bar{\mathbf{d}}$ and $\mathbf{N}$ are given in Appendix A. The displacement vector $\bar{\mathbf{u}}$ is nonlinear as a result of the appropriate beam theory (Trahair 2003).

2.2 Variational formulation and linearisation

The equilibrium equations can be stated in variational form as

$$\delta\bar{\Pi} = \int_L \int_A \delta\bar{\boldsymbol{\varepsilon}}^{\mathrm{T}} \bar{\boldsymbol{\sigma}} \mathrm{d}A \, \mathrm{d}\bar{z} - \delta\bar{\mathbf{d}}^{\mathbf{T}} \bar{\mathbf{f}} = 0 \tag{1}$$

in which A is the cross-sectional area, L is the beam span and $\bar{\mathbf{f}}$ is the external load vector. In Eq. (1), the stress expression can be obtained directly from the strains using the linear elastic stress-strain relationship, i.e., $\bar{\boldsymbol{\sigma}} = \bar{\mathbf{E}}\bar{\boldsymbol{\varepsilon}}$. It should be noted that in order to have free stresses in the contour direction under the rigid cross-section assumption, the beam constitutive matrix $\bar{\mathbf{E}}$ has to be modified as in Appendix A. The first variation of the strain vector for the beam element can be written as

$$\delta\bar{\boldsymbol{\varepsilon}} = \bar{\mathbf{S}}\bar{\mathbf{B}}\delta\bar{\mathbf{d}} \tag{2}$$

where explicit expressions for $\bar{\mathbf{S}}$ and $\bar{\mathbf{B}}$ for an element are given in Appendix A. The incremental equilibrium equations can be obtained by subtracting the virtual work expressions at two neighbouring equilibrium states and then linearising the result by omitting the second- and higher-order terms, i.e.

$$\delta\left(\delta\bar{\Pi}\right) \approx \delta\bar{\mathbf{d}}^{\mathbf{T}}\bar{\mathbf{K}}\delta\bar{\mathbf{d}} - \delta\bar{\mathbf{d}}^{\mathrm{T}}\delta\bar{\mathbf{f}} = 0 \tag{3}$$

where $\overline{\mathbf{K}}$ is the stiffness matrix of the global beam model, i.e.

$$\overline{\mathbf{K}} = \int_L \int_A \overline{\mathbf{B}}^{\mathrm{T}} \overline{\mathbf{S}}^{\mathrm{T}} \mathbf{E} \overline{\mathbf{S}} \overline{\mathbf{B}} \mathrm{d}A \mathrm{d}\overline{z} + \int_L \overline{\mathbf{M}}_{\sigma} \mathrm{d}\overline{z} \tag{4}$$

in which $\overline{\mathbf{M}}_{\sigma} \delta \overline{\mathbf{d}} = \delta \overline{\mathbf{B}}^{\mathrm{T}} \int_A \overline{\mathbf{S}}^{\mathrm{T}} \overline{\boldsymbol{\sigma}} \mathrm{d}A$.

3. Shell-type analysis

3.1 Kinematic assumptions

In this study, the buckling behaviour of thin-walled members is of concern, and thus classical Kirchhoff plate theory is suitable as the plate components align with the first postulate of the beam formulation. In order to conveniently assemble non-coplanar elements to form thin-walled members and folded plates, the Discrete Kirchhoff Quadrilateral (Batoz and Tahar 1982) is employed as the plate component in which shear deformation effects across the thickness are omitted. For the membrane component of the shell-type element, the finite element of (Ibrahimbegovic *et al.* 1990) employing drilling degrees of freedom is adopted. The strains of the shell-type element can be expressed in terms of bending rotations $\hat{\phi}_x$ and $\hat{\phi}_y$ about local $\hat{x}$ and $\hat{y}$ axes and a drilling rotation $\hat{\phi}_z$ about the $\hat{z}$ axis, deflections $\hat{u}_0$ and $\hat{v}_0$ of the mid-surface in the local *x*-*y* plane, and the out-of-plane deflection $\hat{w}_0$ in the local $\hat{z}$ direction (Fig. 2(a)). A standard linear interpolation function is employed for the out of plane deflection $\hat{w}$. The four-node membrane element uses Allman-type interpolation functions for the in-plane displacements $\hat{u}_0$ and $\hat{v}_0$ and standard bilinear interpolation for the independent drilling rotation $\hat{\phi}_z$ (Ibrahimbegovic *et al.* 1990). The details of the shell element interpolation functions can also be found in (Batoz and Tahar 1982, Ibrahimbegovic *et al.* 1990).

3.2 Variational formulation of the equilibrium equations and linearisation

For the shell analysis, the equilibrium equations can be obtained in variational form as

$$\delta \hat{\Pi} = \int_L \int_A \delta \hat{\boldsymbol{\varepsilon}}^{\mathrm{T}} \hat{\boldsymbol{\sigma}} \mathrm{d}A \mathrm{d}\overline{z} - \delta \hat{\mathbf{d}}^{\mathrm{T}} \hat{\mathbf{f}} = 0, \tag{5}$$

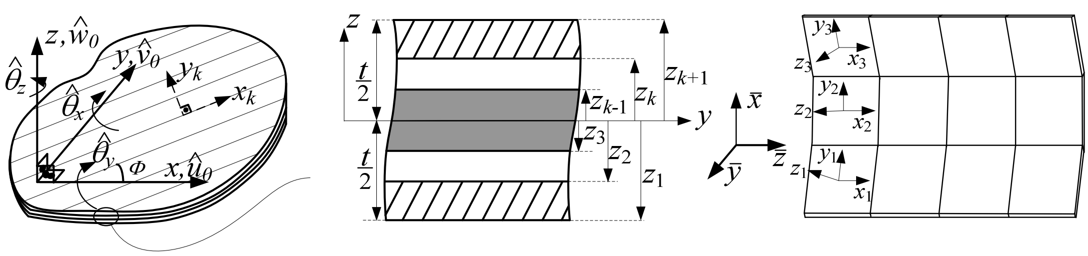

(a) Shell local coordinates (b) Laminates across thickness (c) Global vs. local coordinates

Fig. 2 Deflections and coordinate system of the shell composed of fiber-reinforced laminates in which $\bar{\boldsymbol{\varepsilon}}$ represents the vector of strain components, and an explicit expression for the strain vector for the shell element is given in Appendix B. It should be noted that the strain vector $\bar{\boldsymbol{\varepsilon}}$ of the thin-walled beam formulation can be obtained by substituting the displacement field $\bar{\mathbf{u}}$ (which imposes beam kinematics) into the shell strain expressions $\hat{\boldsymbol{\varepsilon}}$ as given in Appendix B. It should also be noted that the potential energy functional of the shell element is modified in order to avoid numerical stability issues with Allman type interpolations of the membrane component as suggested in Ibrahimbegovic *et al*. (1990), and thus the skew symmetric part of the membrane strains and associated drilling rotations are contained in the first term in Eq. (5). The stress field $\hat{\boldsymbol{\sigma}}$ can be obtained using a linear elastic relationship ($\hat{\boldsymbol{\sigma}}\ \mathbf{E}\boldsymbol{\varepsilon}$) in which $\hat{\boldsymbol{\sigma}}$ and $\overline{\mathbf{E}}$ are also given explicitly in Appendix B. In the last term of Eq. (5), $\hat{\mathbf{f}}$ is the external load vector and $\hat{\mathbf{d}}$ is the vector of nodal displacements. For a thin-walled beam model composed of shell elements, the local shell displacement directions do not generally match with the global (beam) displacement directions; therefore transformation of each degree of freedom to a common global system $\overline{xyz}$ is performed prior to assemblage (Zienkiewicz and Taylor 2000).

The first variation of the strain field of the shell element used in Eq. (5) can be expressed as

$$\delta\hat{\boldsymbol{\varepsilon}} = \hat{\mathbf{S}}\hat{\mathbf{B}}\delta\hat{\mathbf{d}}\ , \tag{6}$$

where $\hat{\mathbf{B}}$, $\hat{\mathbf{S}}$ and $\hat{\mathbf{d}}$ are given explicitly in Erkmen (2013). The incremental equilibrium equations for the shell formulation can be obtained by subtracting the first variation of the modified potential energy in Eq. (5) at two neighbouring equilibrium states and then linearizing the results by omitting the second and higher-order terms, i.e.

$$\delta\left(\delta\hat{\Pi}\right) \approx \delta\hat{\mathbf{d}}^{\mathbf{T}}\hat{\mathbf{K}}\delta\hat{\mathbf{d}} - \delta\hat{\mathbf{d}}^{\mathbf{T}}\delta\hat{\mathbf{f}} = 0\ , \tag{7}$$

where $\hat{\mathbf{K}}$ is the stiffness matrix of the shell model, i.e.

$$\hat{\mathbf{K}} = \int_L\int_A \hat{\mathbf{B}}^{\mathrm{T}}\hat{\mathbf{S}}^{\mathrm{T}}\hat{\mathbf{E}}\hat{\mathbf{S}}\hat{\mathbf{B}}\,\mathrm{d}A\,\mathrm{d}\bar{z} + \int_L \hat{\mathbf{M}}_\sigma\,\mathrm{d}\bar{z}\ , \tag{8}$$

where $\hat{\mathbf{M}}_\sigma\delta\hat{\mathbf{d}} = \delta\hat{\mathbf{B}}^{\mathrm{T}}\int\hat{\mathbf{S}}^{\mathrm{T}}\hat{\boldsymbol{\sigma}}\,\mathrm{d}A$.

4. Iterative global-local procedure

4.1 Domain decomposition and coarse-scale projection

The proposed global-local/multi-scale analysis is performed only in a critical region of the analysis domain depicted as Ω_m in Fig. 3. In the multi-scale analysis domain, the beam and shell models overlap. The whole analysis domain including Ω_m is represented with Ω_c in Fig. 3; a beam model being used for the whole analysis domain Ω_c. Following the Bridging multiscale method of Liu and his co-workers, the shell nodal displacement vector is decomposed into a coarse-scale component and a difference term, by using a decomposition matrix $\mathbf{N}$ that projects the beam solution onto the nodal points of the shell model, i.e., $\hat{\mathbf{d}} = \mathbf{N}\bar{\mathbf{d}} + \mathbf{d}'$, from which the variation of the shell nodal displacement vector can be written as

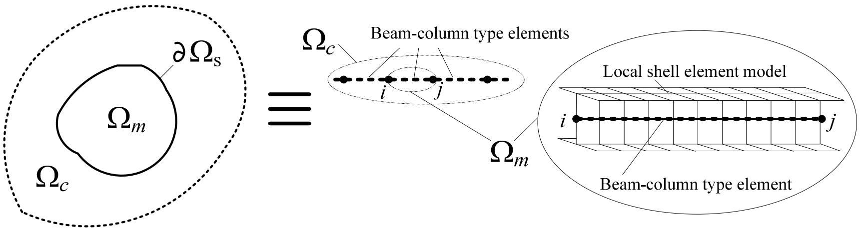

Fig. 3 Decomposition of the analysis domain

$$\delta\hat{\mathbf{d}} = \mathbf{N}\delta\overline{\mathbf{d}} + \delta\mathbf{d}', \tag{9}$$

4.2 Coupled coarse- and fine-scale equilibrium equations

Based on the above decomposition of the shell solution, and thus by substituting Eq. (9) into Eq. (6), i.e., $\delta\hat{\boldsymbol{\varepsilon}} = \hat{\mathbf{S}}\hat{\mathbf{B}}\left(\mathbf{N}\delta\overline{\mathbf{d}} + \delta\mathbf{d}'\right)$, the first variation of the shell strains can be decomposed as

$$\delta\overline{\boldsymbol{\varepsilon}}=\hat{\mathbf{S}}\hat{\mathbf{B}}\mathbf{N}\delta\overline{\mathbf{d}}, \tag{10}$$

and

$$\delta\boldsymbol{\varepsilon}' =\hat{\mathbf{S}}\hat{\mathbf{B}}\delta\mathbf{d}'. \tag{11}$$

As the beam kinematics is imposed by using $\mathbf{N}$, the variation of the coarse scale strain component of the shell solution $\delta\overline{\boldsymbol{\varepsilon}}$ is equal to that of the beam, i.e., $\hat{\mathbf{S}}\hat{\mathbf{B}}\mathbf{N} = \overline{\mathbf{S}}\overline{\mathbf{B}}$. In Eq. (11), $\delta\boldsymbol{\varepsilon}'$ is due to the difference between the variations of the fine and coarse-scale strain fields. The strain field $\hat{\boldsymbol{\varepsilon}}$ can also be decomposed into two components, i.e., $\hat{\boldsymbol{\varepsilon}} = \overline{\boldsymbol{\varepsilon}} + \boldsymbol{\varepsilon}'$. Herein, the coarse-scale strain field $\overline{\boldsymbol{\varepsilon}}$ is such that its variation is as in Eq. (10). Thus, it is equal to the strain field of the beam solution. The stress field is also decomposed into two components i.e., $\hat{\boldsymbol{\sigma}} = \overline{\boldsymbol{\sigma}} + \boldsymbol{\sigma}'$. and considering linear elastic constitutive relations, the stress field components can be obtained from the associated strain fields, i.e., $\hat{\boldsymbol{\sigma}} = \hat{\mathbf{E}}\boldsymbol{\varepsilon}$ and $\overline{\boldsymbol{\sigma}} = \overline{\mathbf{E}}\overline{\boldsymbol{\varepsilon}}$. By substituting the above equations into Eq. (5), the weak form of the shell equilibrium equations can be decomposed as

$$\delta\Pi_1 = \delta\overline{\mathbf{d}}^{\mathrm{T}}\mathbf{N}^{\mathrm{T}}\int_L\int_A \hat{\mathbf{B}}^{\mathrm{T}}\hat{\mathbf{S}}^{\mathrm{T}}\overline{\boldsymbol{\sigma}}\mathrm{d}A\mathrm{d}\overline{z} - \delta\overline{\mathbf{d}}^{\mathrm{T}}\mathbf{N}^{\mathrm{T}}\hat{\mathbf{f}} + \delta\overline{\mathbf{d}}^{\mathrm{T}}\mathbf{F} = 0 \tag{12}$$

and

$$\delta\Pi_2 = \delta\mathbf{d}'^{\mathrm{T}}\int_L\int_A \hat{\mathbf{B}}^{\mathrm{T}}\hat{\mathbf{S}}^{\mathrm{T}}\hat{\boldsymbol{\sigma}}\mathrm{d}A\mathrm{d}\overline{z} - \delta\mathbf{d}'^{\mathrm{T}}\,\mathbf{f} = 0. \tag{13}$$

It should be noted that within the BMM, the coarse- and fine-scale decomposition is applied on the discrete nodal values, and thus the relation $\int\int \mathbf{N}^{\mathrm{T}}\hat{\mathbf{B}}^{\mathrm{T}}\hat{\mathbf{S}}^{\mathrm{T}}\boldsymbol{\sigma}\mathrm{d}A\mathrm{d}\overline{z} = \mathbf{N}^{\mathrm{T}}\int\int \hat{\mathbf{B}}^{\mathrm{T}}\hat{\mathbf{S}}^{\mathrm{T}}\boldsymbol{\sigma}\mathrm{d}A\mathrm{d}\overline{z}$ can be used. By considering a load case where $\mathbf{N}^{\mathrm{T}}\hat{\mathbf{f}} = \overline{\mathbf{f}}$, the first two terms in Eq. (12) can be replaced with those of Eq. (1). What separates the beam equations given in Eq. (1) from Eq. (12) is the last term, in which $\mathbf{F}$ is a complementary force vector due to fine- and coarse-scale differences in the stress field, which can be written explicitly as

$$\mathbf{F} = \mathbf{N}^{\mathrm{T}} \int_L \int_A \hat{\mathbf{B}}^{\mathrm{T}} \hat{\mathbf{S}}^{\mathrm{T}} \left(\hat{\boldsymbol{\sigma}} - \bar{\boldsymbol{\sigma}} \right) \mathrm{d}A\mathrm{d}\bar{z} = \int_L \int_A \bar{\mathbf{B}}^{\mathrm{T}} \bar{\mathbf{S}}^{\mathrm{T}} \boldsymbol{\sigma}' \mathrm{d}A\mathrm{d}\bar{z} \,. \tag{14}$$

4.3 Linearisation of the equilibrium equations

Linearisation of Eq. (12) produces

$$\delta\left(\delta\Pi_1\right) \approx \delta\bar{\mathbf{d}}^{\mathrm{T}} \bar{\mathbf{K}} \delta\bar{\mathbf{d}} + \delta\bar{\mathbf{d}}^{\mathrm{T}} \delta\mathbf{F} = 0 \,, \tag{15}$$

where

$$\bar{\mathbf{K}} = \mathbf{N}^{\mathrm{T}} \left(\int_L \int_A \hat{\mathbf{B}}^{\mathrm{T}} \hat{\mathbf{S}}^{\mathrm{T}} \bar{\mathbf{E}} \hat{\mathbf{S}} \hat{\mathbf{B}} \mathrm{d}A\mathrm{d}\bar{z} + \int_L \tilde{\mathbf{M}}_\sigma \mathrm{d}\bar{z} + \int_L \tilde{\mathbf{M}}_s \mathrm{d}\bar{z} \right) \mathbf{N} \tag{16}$$

and can be replaced with the beam stiffness matrix in Eq. (4), in which $\tilde{\mathbf{M}}_\sigma$ is defined in

$$\tilde{\mathbf{M}}_\sigma \delta\hat{\mathbf{d}} = \delta\hat{\mathbf{B}}^{\mathrm{T}} \int_A \hat{\mathbf{S}}^{\mathrm{T}} \bar{\mathbf{E}} \hat{\boldsymbol{\varepsilon}} \mathrm{d}A \tag{17}$$

and $\tilde{\mathbf{M}}_s$ is defined in

$$\mathbf{N}^{\mathrm{T}} \tilde{\mathbf{M}}_s \delta\hat{\mathbf{d}} = \delta\mathbf{N}^{\mathrm{T}} \hat{\mathbf{B}}^{\mathrm{T}} \int_A \hat{\mathbf{S}}^{\mathrm{T}} \bar{\mathbf{E}} \hat{\boldsymbol{\varepsilon}} \mathrm{d}A \,. \tag{18}$$

In obtaining Eq. (15), the difference between the nodal displacements of fine- and coarse-scales was defined as $\delta\mathbf{d}' = \mathbf{N}\delta\mathbf{c} + \mathbf{Q}\delta\mathbf{q}$, in which $\delta\mathbf{c}$ can be selected as

$$\delta\mathbf{c} = -\left[\mathbf{N}^{\mathrm{T}} \left(\hat{\mathbf{K}} + \int_L \left(\tilde{\mathbf{M}}_s + \mathbf{k}_s \right) \mathrm{d}\bar{z} \right) \mathbf{N} \right]^{-1} \mathbf{N}^{\mathrm{T}} \int_L \left(\mathbf{k} + \mathbf{k}_\sigma + \mathbf{k}_s \right) \mathrm{d}\bar{z} \mathbf{N} \delta\bar{\mathbf{d}} \,, \tag{19}$$

in which $\hat{\mathbf{K}}$ is as given in Eq. (8) and

$$\mathbf{k} = \int_A \hat{\mathbf{B}}^{\mathrm{T}} \hat{\mathbf{S}}^{\mathrm{T}} \left(\hat{\mathbf{E}} - \bar{\mathbf{E}} \right) \hat{\mathbf{S}} \hat{\mathbf{B}} \mathrm{d}A \,; \tag{20a}$$

$$\mathbf{k}_\sigma \delta\hat{\mathbf{d}} = \delta\hat{\mathbf{B}}^{\mathrm{T}} \int_A \hat{\mathbf{S}}^{\mathrm{T}} \left(\hat{\mathbf{E}} - \bar{\mathbf{E}} \right) \hat{\boldsymbol{\varepsilon}} \mathrm{d}A \tag{20b}$$

$$\mathbf{N}^{\mathrm{T}} \mathbf{k}_s \delta\hat{\mathbf{d}} = \delta\mathbf{N}^{\mathrm{T}} \hat{\mathbf{B}}^{\mathrm{T}} \int_A \hat{\mathbf{S}}^{\mathrm{T}} \left(\hat{\mathbf{E}} - \bar{\mathbf{E}} \right) \hat{\boldsymbol{\varepsilon}} \mathrm{d}A \,, \tag{20c}$$

The matrix $\mathbf{Q}$ can be selected as

$$\mathbf{Q} = \mathbf{I} - \mathbf{N} \left[\mathbf{N}^{\mathrm{T}} \left(\hat{\mathbf{K}} + \int_L \left(\tilde{\mathbf{M}}_s + \mathbf{k}_s \right) \mathrm{d}\bar{z} \right) \mathbf{N} \right]^{-1} \mathbf{N}^{\mathrm{T}} \left(\hat{\mathbf{K}} + \int_L \left(\tilde{\mathbf{M}}_s + \mathbf{k}_s \right) \mathrm{d}\bar{z} \right), \tag{21}$$

so that there is an orthogonality relation between $\mathbf{N}$ and $\mathbf{Q}$ (Qian *et al.* 2004), i.e.

$$\mathbf{N}^{\mathrm{T}}\left(\hat{\mathbf{K}}+\int_{L}\left(\tilde{\mathbf{M}}_{s}+\mathbf{k}_{s}\right)\mathrm{d}\overline{z}\right)\mathbf{Q}=0\,, \tag{22}$$

On the other hand, linearisation of Eq. (13) produces

$$\delta\left(\delta\Pi_{2}\right)\approx\delta\mathbf{d}'^{\mathrm{T}}\hat{\mathbf{K}}\delta\hat{\mathbf{d}}-\delta\mathbf{d}'^{\mathrm{T}}\delta\hat{\mathbf{f}}=0\cdot \tag{23}$$

Since $\delta\mathbf{d}'$ in Eq. (23) is arbitrary, both Eqs. (7)-(23) admit the same solution, which is the solution of the shell model over the entire analysis domain. However, where the beam solution is accurate enough, the shell model solution is avoided for computational economy.

4.4 Interface boundary conditions and partitioning of the linearised fine-scale equations

In the original applications of the Bridging Multi-scale Method, e.g., (Kadowaki and Liu 2004) the coarse-scale solution within the overlapping domain is used to obtain the difference between the fine and coarse-scale displacements. Instead, herein it is more convenient to obtain the shell solution within the overlapping domain by imposing the displacements of the beam solution as the interface boundary conditions of the shell model. One important issue to be addressed before imposing the shell boundary conditions is that even though there are no local buckling deformations, the Poisson's ratio effect causes change in the cross-sectional contour dimensions throughout the analysis domain. However, beam analysis does not produce a displacement field within the plane of the cross-section that captures the changes in cross-sectional dimensions due to Poisson's ratio effect. On the other hand, as explained in Section 2.2, this effect is considered in the stress field by adopting a separate constitutive matrix. Indeed, within the analysis region where the beam solution is deemed accurate, a strain field is imposed implicitly which can be considered within the current analysis framework as the fine-scale strain component in the beam solution, i.e., $\boldsymbol{\varepsilon}'=\left\langle 0 \quad -\varepsilon\,\overline{Q}_{12}^{(k)}/\overline{Q}_{22}^{(k)} \quad 0 \quad 0\right\rangle^{\mathrm{T}}$, in which ε indicates the axial strain in the coarse-scale strain vector, and material properties $\overline{Q}_{12}^{(k)}$ and $\overline{Q}_{22}^{(k)}$ are as given in Lee *et al.* (2002). It is important to note that this fine-scale strain field has no influence on the beam equilibrium equations and the coarse-scale nodal displacement vector, because the associated fine-scale stress field is a null vector. This was provided by decomposing the stress field using the stress-strain relations as $\hat{\boldsymbol{\sigma}}=\hat{\mathbf{E}}\hat{\boldsymbol{\varepsilon}}$ and $\overline{\boldsymbol{\sigma}}=\overline{\mathbf{E}}\overline{\boldsymbol{\varepsilon}}$. Therefore, consideration of the fine-scale strain field $\boldsymbol{\varepsilon}'=\left\langle 0 \quad -\varepsilon\,\overline{Q}_{12}^{(k)}/\overline{Q}_{22}^{(k)} \quad 0 \quad 0\right\rangle^{\mathrm{T}}$ is required only at the interface of the multi-scale region ($\partial\Omega_s$ in Fig. 3), in order to consider the changes in the cross-sectional contour dimensions before imposing the shell model boundary conditions. The reason for not including the strains due to Poisson's ratio effects in the coarse-scale strain vector is the convenience of the coarse-scale decomposition matrix $\mathbf{N}$ based on the kinematic considerations under a rigid sectional contour assumption. At both ends of the shell model, the fine scale displacement vector due to Poisson's ratio effect $\tilde{\mathbf{d}}_{@i\&j}$ is obtained by integrating the strains numerically, i.e., $-\nu\varepsilon$, over the cross-sectional contour, and then by imposing the condition that the summation of these displacements vanishes in order to eliminate the rigid body translations due to $\tilde{\mathbf{d}}_{@i\&j}$. Thus, the displacement boundary conditions imposed onto the shell model can be written as $\hat{\mathbf{d}}_{@i\&j} \approx \mathbf{N}\bar{\mathbf{d}}_{@i\&j}\tilde{\mathbf{d}}_{@i\&j}$ where subscripts "*i&j*" indicate both ends of the local shell model as shown in Fig. 3. From Eq. (23), decomposing the shell displacement vector into boundary and internal displacement vectors produces

$$\underbrace{\left[\begin{array}{c|c} \hat{\mathbf{K}}_a & \hat{\mathbf{K}}_b \\ \hline \hat{\mathbf{K}}_b^{\mathrm{T}} & \hat{\mathbf{K}}_c \end{array}\right]}_{\hat{\mathbf{K}}} \underbrace{\left\{\begin{array}{c} \boxed{\delta\hat{\mathbf{d}}_{@i\&j}} \\ \hline \delta\hat{\mathbf{d}}_{IN} \end{array}\right\}}_{\delta\hat{\mathbf{d}}} = \underbrace{\left\{\begin{array}{c} \delta\hat{\mathbf{f}}_{@i\&j} \\ \hline \boxed{\delta\hat{\mathbf{f}}_s} \end{array}\right\}}_{\delta\hat{\mathbf{f}}}. \tag{24}$$

The stiffness matrix $\hat{\mathbf{K}}$ of the shell model in Eq. (8), is partitioned such that specified boundary displacements are multiplied with the sub-matrix $\hat{\mathbf{K}}_b^T$. In Eq. (24), $\delta\hat{\mathbf{f}}_s$ is the vector of variations in specified external loads that falls into the multi-scale analysis domain and $\delta\hat{\mathbf{f}}_{@i\&j}$ is the vector of variations in the traction forces at the boundaries of the multi-scale analysis domain. Specified displacements and loads in Eq. (24) are placed in the box symbol (□).

4.5 Solution procedure for the nonlinear equilibrium equations

Firstly, the global problem is solved for the coarse-scale displacements $\bar{\mathbf{d}}$ while keeping the fine-scale solution of the local shell model fixed. Then, given the global results imposed on the local model as the interface boundary conditions, the local problem is solved for the fine-scale values $\hat{\mathbf{d}}$, while keeping the boundary conditions and the global displacements $\bar{\mathbf{d}}$ fixed. In order to terminate the loading step *k*, double criteria as suggested in Qian *et al*. (2004) are used within the framework of the BMM. The first criterion is due to geometric nonlinearity, and confirms that the nonlinear global equilibrium condition is satisfied at the end of *n* iterations. An additional second criterion is required to confirm that the difference between the stress vectors of the local shell model and the beam model is eliminated through the complementary force in Eq. (14); thus the local and global solutions are synchronized. A flow chart of the solution procedure is given in Fig. 4.

The global equations are solved using a Newton-Raphson incremental-iterative scheme in a step-by-step manner, i.e.

$$\bar{\mathbf{K}}_k \Delta\bar{\mathbf{d}}_k^n = \Delta\bar{\mathbf{f}}_k + \Delta\bar{\mathbf{R}}_k^n \tag{25}$$

where $\bar{\mathbf{K}}_k$ is the tangent stiffness matrix at the beginning of each incremental step, $\Delta\bar{\mathbf{f}}_k$ is the external load increment in step *k*, and $\Delta\bar{\mathbf{R}}_k^n$ is the unbalanced force vector obtained from Eq. (12) at the n^{th} iteration of step *k*, i.e.

$$\Delta\bar{\mathbf{R}}_k^n = -\int_L\int_A \bar{\mathbf{B}}_k^{n\mathrm{T}}\bar{\mathbf{S}}^{\mathrm{T}}\bar{\boldsymbol{\sigma}}_k^n \mathrm{d}A\mathrm{d}\bar{z} - \mathbf{F}_k^n + \bar{\mathbf{f}}_k \ . \tag{26}$$

It should also be noted that on the right hand side of Eq. (25), $\Delta\bar{\mathbf{f}}_k$ is used for the first iteration, and $\Delta\bar{\mathbf{R}}_k^n$ is used after the first iteration until convergence is reached within the step in the usual manner. Displacements of the current state are updated using the incremental nodal displacements, i.e., $\bar{\mathbf{d}}_k^n = \bar{\mathbf{d}}_k^{n-1} + \Delta\bar{\mathbf{d}}_k^n$, based on which the internal strain field, i.e., $\bar{\boldsymbol{\varepsilon}}_k^n = \mathbf{B}\bar{\mathbf{d}}_k^n$ and consequently the stress field, i.e., $\bar{\boldsymbol{\sigma}}_k^n = \mathbf{E}\bar{\boldsymbol{\varepsilon}}_k^n$ of the coarse-scale solution can also be updated. Within the global load

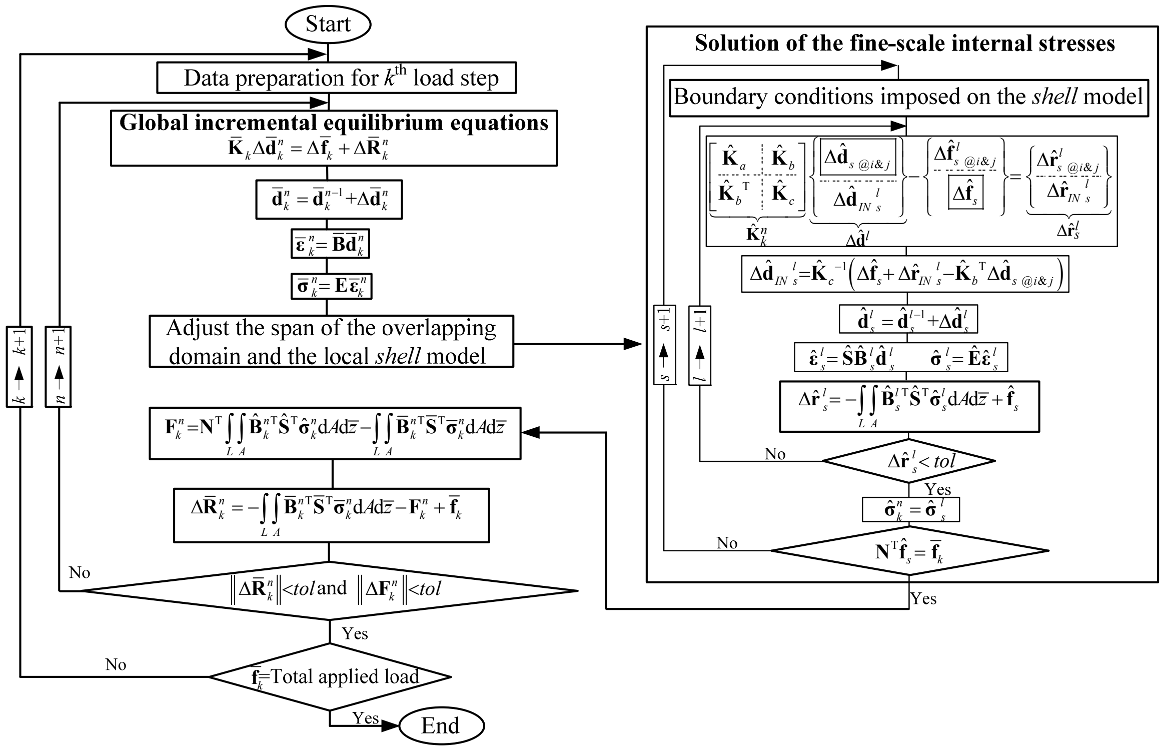

Fig. 4 Flow-chart of the multi-scale analysis algorithm

step k, the local shell model is solved in s steps in which displacement increments of the internal nodes are determined for l iterations, i.e., $\Delta\hat{\mathbf{d}}_{IN\,s}^{\;l}$, because the unbalanced terms due to the geometric nonlinearities, i.e., $\Delta\hat{\mathbf{r}}_{IN\,s}^{\;l}$ are also corrected in the local shell model in an iterative manner. Thus, from the second line of Eq. (24), this fine-scale displacement vector of the internal nodes at the l^{th} iteration $\Delta\hat{\mathbf{d}}_{IN\,s}^{\;l}$ can be written as

$$\Delta\hat{\mathbf{d}}_{IN\,s}^{\;l}=\hat{\mathbf{K}}_c^{-1}\left(\Delta\hat{\mathbf{f}}_s+\Delta\hat{\mathbf{r}}_{IN\,s}^{\;l}-\hat{\mathbf{K}}_b^{\mathrm{T}}\Delta\hat{\mathbf{d}}_{s\,@i\&j}\right), \tag{27}$$

in which $\Delta\hat{\mathbf{d}}_{s@i\&j}$ indicates the specified displacement increments at the boundaries of the fine-scale domain. In Eq. (27), $\Delta\hat{\mathbf{r}}_{IN\,s}^{\;l}$ is the unbalanced load vector due to geometric nonlinearities involved in the local shell problem, which can be obtained as

$$\Delta\hat{\mathbf{r}}_s^{\,l}=-\int_L\int_A \hat{\mathbf{B}}_s^{l\,\mathrm{T}}\hat{\mathbf{S}}^{\mathrm{T}}\hat{\boldsymbol{\sigma}}_s^{l}\,\mathrm{d}A\mathrm{d}\overline{z}+\hat{\mathbf{f}}_s\,. \tag{28}$$

The incremental shell nodal displacements obtained from Eq. (27) are used in updating the displacement configuration of the current state, i.e., $\hat{\mathbf{d}}_s^{l}=\hat{\mathbf{d}}_s^{l-1}+\Delta\hat{\mathbf{d}}_s^{l}$, based on which the internal strain field $\hat{\boldsymbol{\varepsilon}}_s^{l}$ and consequently the stress field $\hat{\boldsymbol{\sigma}}_s^{l}$ of the fine-scale solution can be updated. If the local convergence criterion is satisfied, i.e., $\left\|\Delta\hat{\mathbf{r}}_s^{l}\right\|<\varepsilon_{tol}$ then $\hat{\boldsymbol{\sigma}}_k^{n}=\hat{\boldsymbol{\sigma}}_s^{\,l}$ is used for the complementary force calculations within the k^{th} step in each n^{th} iteration, i.e.

$$\mathbf{F}_k^n = \mathbf{N}^{\mathrm{T}} \int_L \int_A \hat{\mathbf{B}}_k^{n\mathrm{T}} \hat{\mathbf{S}}^{\mathrm{T}} \hat{\boldsymbol{\sigma}}_k^n \mathrm{d}A\mathrm{d}\overline{z} - \int_L \int_A \overline{\mathbf{B}}_k^{n\mathrm{T}} \overline{\mathbf{S}}^{\mathrm{T}} \overline{\boldsymbol{\sigma}}_k^n \mathrm{d}A\mathrm{d}\overline{z} \,. \tag{29}$$

It should be noted that for a stable global system the global equilibrium should be satisfied for any complementary force vector. Therefore, even though the convergence criterion for global equations is reached, i.e., $\left\|\Delta\overline{\mathbf{R}}_k^n\right\| < \varepsilon_{tol}$, step k is not deemed complete unless $\left\|\Delta\mathbf{F}_k^n\right\| < \varepsilon_{tol}$ is satisfied, so that the local and global solutions are synchronised. If both convergence criteria are not satisfied, the analysis should be repeated for a reduced load increment within the same step k. It should also be noted that within the multi-scale analysis scheme developed herein, the span of the overlapping domain can be adjusted at any load level, because the local shell model is solved for the current loading conditions at the beginning of each step, regardless of the results of the shell model obtained in the previous steps.

5. Numerical examples

As discussed previously, the iterative global-local procedure is most advantageous when a limited portion of the member domain is affected by localized/cross-sectional deformations. Therefore, the accuracy and efficiency of proposed multi-scale procedure is verified through numerical examples in which local deformations cause a softening effect in the global behaviour of the structure. In all of the examples, the accuracy of the model is checked by comparing the results of the multi-scale model with that of a full shell element. However, the accuracy of the developed shell element needs to be confirmed before being used as a benchmark. Consequently, the first three examples are presented to compare the buckling load obtained from the present model to the results from literature for various materials and loading conditions. It should be noted that the critical load values presented herein are obtained from a nonlinear analysis and are defined as load level that minimizes the determinant of the tangential stiffness matrix of the structure as depicted in Fig. 5. The rest of the examples are designed to express the accuracy and efficiency of the proposed global-local model. In the first example, an isotropic material (structural steel) is used while orthotropic graphite- and glass-epoxy composite laminates are used in the rest of the examples.

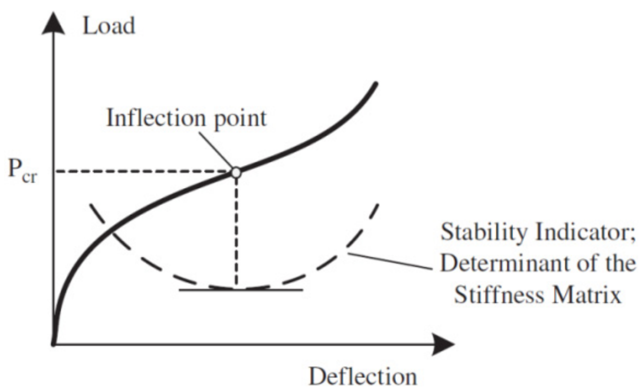

Fig. 5 Definition of the buckling criteria in the nonlinear analysis

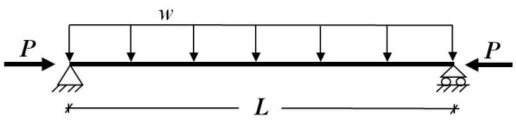

(a) Loading and boundary conditions

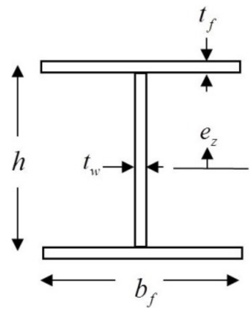

(b) Cross-sectional dimensions

Fig. 6 Simply-supported beam

Table 1 Buckling load for isotropic simply supported beam

Load case	Machado (2010)	Present	Difference (%)
Axial (KN)	766.05	771.75	0.74
Lateral $e_z = h/2$ (MNm)	121.8	122.06	0.21
Lateral $e_z = -h/2$ (MNm)	240.4	244.1	1.52

5.1 Verification of the shell element

5.1.1 Example 1: Isotropic simply supported I-beam

In order to verify the developed shell element, a simply supported I-beam made of isotropic material is analysed in example 1. Cross-sectional properties, loading and boundary conditions are shown in Fig. 6. Geometrical dimensions of the I-section are $b_f = 200$ mm, $h = 195$ mm, $t_f = 10$ mm and $t_w = 6.5$ mm, and the length of the beam is $L = 6000$ mm. Material properties corresponding to construction steel (i.e., $E = 200$ GPa and $\nu = 0.3$) is used, and the beam is subjected to axial load and uniformly distributed lateral load.

Full nonlinear shell analysis is performed to obtain the buckling load as discussed previously, and the results are checked against the buckling results presented by Machado (2010). The buckling load is calculated for the simply supported beam subjected to axial and uniformly distributed lateral load. Two cases were analysed for the uniformly distributed load: firstly, the load was applied at the top flange and in a separate analysis, the load was applied on the bottom flange, which are denoted by $e_z = h/2$ and $e_z = -h/2$, respectively. The buckling loads are shown in Table 1, where for the lateral load, the results are presented in terms of the corresponding maximum bending moment.

The axial buckling load can also be calculated from the Euler formula $P_{cr} = \pi^2 E / (L)^2$, where L is the length of the beam and EI is the flexural rigidity of the section about the minor principal axis. Using the properties of the member in this example, the Euler buckling load is calculated as 767.9 kN. It can be observed that the buckling load values obtained from the developed shell formulation are in good agreement with the results from the literature.

5.1.2 Example 2: Composite laminate simply-supported I-beam subjected to distributed load

The lateral-torsional buckling behaviour of a laminated simply-supported I-beam is investigated

Table 2 Material properties of composite laminates

Material	E_1	E_2	G_{12}	v_{12}	v_{21}
Graphite-epoxy	144 GPa	9.65 GPa	4.14 GPa	0.3	0.02
Glass-epoxy	48.3 GPa	19.8 GPa	8.96 GPa	0.27	0.11

Table 3 Buckling load for composite simply-supported beam under distributed load

	Graphite/Epoxy		Glass/Epoxy	
Load level	Machado (2010)	Present	Machado (2010)	Present
$e_z = h/2$	0.25	0.25	0.12	0.12
$e_z = 0$	0.42	0.40	0.18	0.18
$e_z = -h/2$	0.67	0.63	0.26	0.24

in this example. The beam length and the boundary conditions are the same as the previous example, and the geometrical dimensions of the cross-section are: $b_f = 300$ mm, $h = 600$ mm and $t_f = t_w = 30$ mm (Fig. 6). The analysis is performed for two types of material; namely, graphite-epoxy and glass-epoxy composite laminates, properties of which can be seen in Table 2.

The plates are made up of four layers of composite material, each of which have a thickness of 7.5 mm, with a stacking sequence of [0/0/0/0]. The uniformly distributed load is applied at three levels: the top flange, the shear centre and the bottom flange, which are depicted by $e_z = h/2$, $e_z = 0$ and $e_z = -h/2$, respectively. Similar to the previous example, the buckling load levels are obtained from the nonlinear shell analysis by drawing the lateral deflection versus the load level and considering the load level at which the tangential stiffness of the structures is minimum, and the results are compared to the buckling loads reported by Machado (2010) for verification purposes. The results can be seen in Table 3 in terms of the values of the distributed load (in MN/m) causing the buckling behaviour. Like the previous example, a good agreement can be confirmed between the results of the adopted shell model and results from the literature.

5.1.3 Example 3: *Effect of fibre orientation on buckling behaviour of composite laminate columns*

In order to verify the accuracy of the developed shell element in capturing the effects of fibre orientation in composite laminates, simply-supported columns with various fibre orientation angles are analyzed in this example. The cross-section is a doubly-symmetric I with the following dimensions: $b_f = 80$ mm, $h = 40$mm and $t_f = t_w = 1$ mm (Fig. 6). The length of the beam is $L = 240$ mm, and the boundary conditions are similar to the previous examples. The column is composed of eight layers of graphite-epoxy composite laminates (Table 4) each $d = 0.25$ mm thick, with stacking sequence $[\theta/-\theta/\theta/-\theta]_s$. $-\theta$ is the angle between the fibres and the axis of the beam, and is selected as 15°, 30°, 45°, 60°, 75° and 90°.

Table 4 Material properties for Example 3

Material	E_1	E_2	G_{12}	v_{12}	v_{21}
Graphite-epoxy	138 GPa	10 GPa	5 GPa	0.27	0.02

Table 5 Buckling load for simply-supported column, various fibre angles

θ	15°	30°	45°	60°	75°	90°
Present study	14.67	25.00	29.70	24.09	14.19	9.35
Mittelstedt (2007)	14.75	23.20	27.70	22.75	13.71	9.41

Table 6 Values of material properties used in Section 6.2

Material	E_1	E_2	G_{12}	v_{12}	v_{21}
Glass-epoxy	53.78 GPa	17.93 GPa	8.96 GPa	0.25	0.08

In order to obtain the buckling load of the column, a nonlinear shell analysis is performed by adopting shell element of 20 mm × 20 mm size. The results of the analysis in comparison with the buckling results presented by Mittelstedt (2007) can be observed in Table 5. It can be observed from the results that the accuracy of the developed shell element for the analysis of composite laminates can be confirmed.

5.2 Verification of the proposed global-local method

In the following, numerical experiments are performed in order to demonstrate the accuracy and efficiency of the proposed global-local/multi-scale procedure in capturing the effect of localized behaviour. The results of the multi-scale method are compared with the beam and shell results for verification purposes. The material is taken as glass-epoxy, for which the material properties are provided in Table 6.

5.2.1 Flexural buckling of a C-shaped column

The multiscale procedure is used to analyze the buckling behaviour of the composite column shown in Fig. 7.

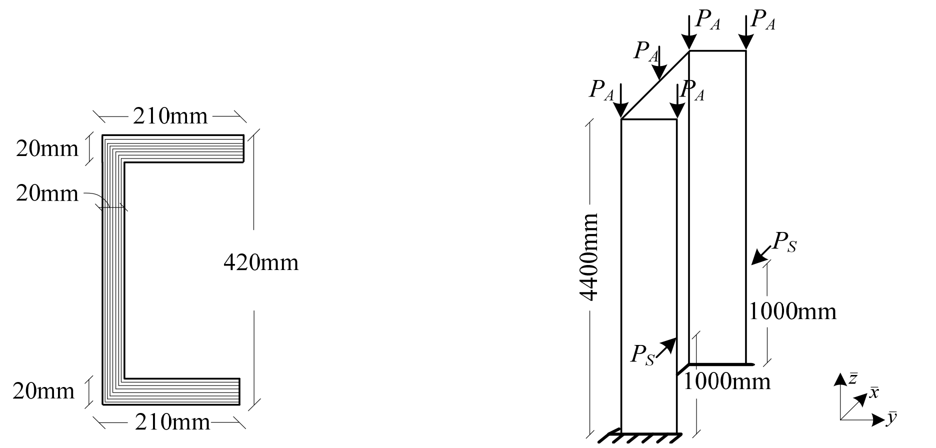

(a) Cross-sectional dimensions (b) Loading and boundary conditions

Fig. 7 C-section composite column

Table 7 Buckling load values for C-section column

Analysis	Beam	Constraint shell	Shell	Closed-from (Euler)
Buckling load (kN)	52.19	52.12	53.48	51.93

The beam is composed of eight composite layers with equal thickness of 2.5 mm with a stacking sequence of $[0/\text{-}45/90/45]_{S.}$ The analysis is performed using the beam-type element, the shell-type element and the multiscale procedure. Apart from that, a constraint shell model is used to confirm that the beam-type analysis and the shell model are kinematically equivalent according to the kinematic assumptions of the thin-walled beam theory. It is obtained by applying multi-point constraints (MPSs) on the nodal displacements of the shell model in each cross-section according to the decomposition matrix **N**. For beam analysis, 4 equal-span elements are used while the dimensions of the shell elements are approximately 200 mm × 200 mm.

The loading set presented in Fig. 7 is applied at two stages; initially, the axial/vertical loads are applied (i.e., $P_s = 0$). The values of the buckling load are calculated using the linearized buckling analysis corresponding to beam, constrain-shell and full-shell and are presented in Table 7. The close-form solution presented in the same table is the Euler buckling load, which is calculated from $N_{cr} = \pi^2 E / (2L)^2$, where L is the length of the column and EI is the flexural rigidity of the cross-section around the minor principal axis. Additionally, nonlinear analysis are performed using the aforementioned finite element models and the results are depicted in Fig. 8 in terms of horizontal deflection and rotation of the tip of the column versus the applied load. It can be observed that the results of all of the models match at this stage.

At a second stage, local/cross-sectional deformations are introduced to the model by assigning $P_s = 75$ kN. It should be noted that the P_s load couple cancel the effect of each other at cross-sectional level. Consequently, the beam-type finite element, which is formulated based on rigid cross-sectional assumption, fails to capture the effect of this load couple on the behaviour of the column. However, the softening effect of the local deformations in significant on the global response of the column, as shown by the curved obtained from the full shell model (Fig. 8).

The above problem is also analyzed using the developed multi-scale model that is composed of

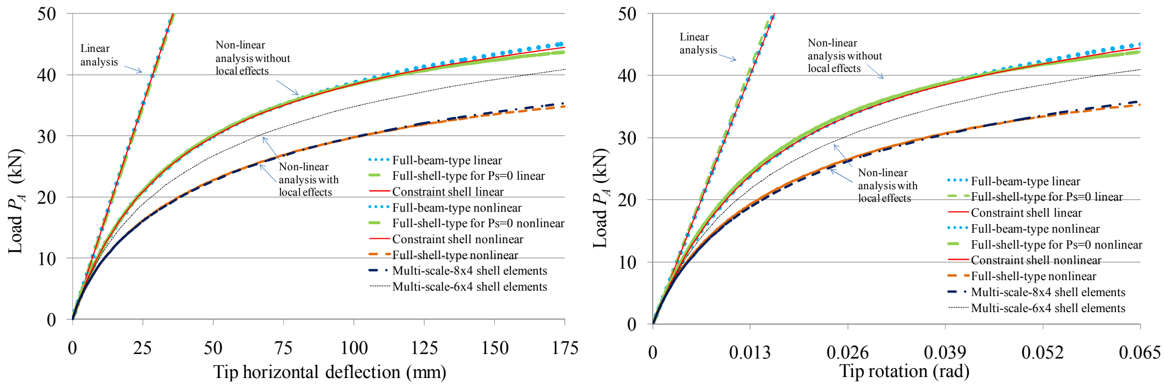

(a) Tip horizontal deflection (b) Tip rotation

Fig. 8 Load-displacement curves based on various finite element modelling

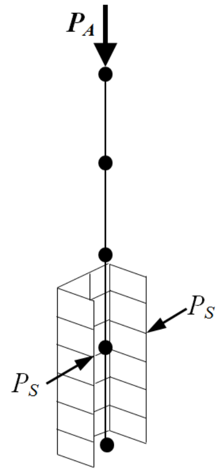

Fig. 9 Layout of the multi-scale model

beam and shell elements. The layout of the multi-scale model is shown in Fig. 9. The model is analyzed by considering two values for the length of the overlapping region: initially it was considered between z = 0 and z = 1200 mm by using 6×4 shell elements, and then it was expanded to cover z = 0 and z = 1600 mm by using 8×4 elements. The results of the multi-scale analysis are shown in Fig. 8. It can be seen that the model with larger overlapping region (i.e., 8×4 elements) has been able to capture the effect of localized behaviour accurately and is matching well with the full shell model. On the other hand, the model with smaller shell span is not able to fully capture the effect. It should be noted that even the model with larger shell span has considerably smaller number of shell elements and therefore smaller number of degrees of freedom compared to the full shell model. Therefore, the accuracy and the efficiency of the proposed model can be verified herein. Care should be taken in choosing the overlapping region to ensure that it covers the entire region affected by the localized behaviour.

5.2.2 Lateral-torsional buckling of an I-beam

The effect of a localized load couple on the lateral-torsional buckling resistance of a simply-supported I-beam is studied in this section. The geometry, boundary conditions and loading of the beam are shown in Fig. 10.

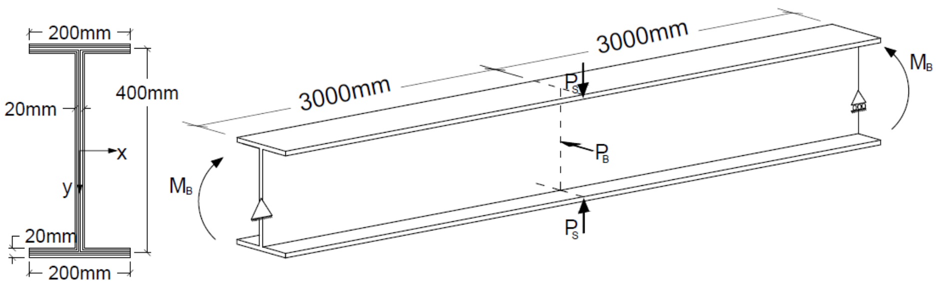

(a) Cross-sectional dimensions (b) Loading and boundary conditions

Fig. 10 Properties of the simply supported I-beam

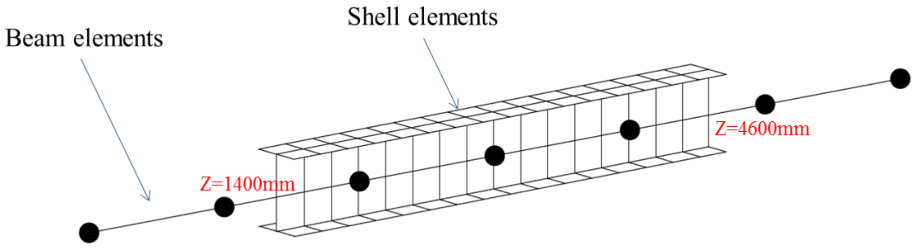

Fig. 11 Schematic of the multi-scale model

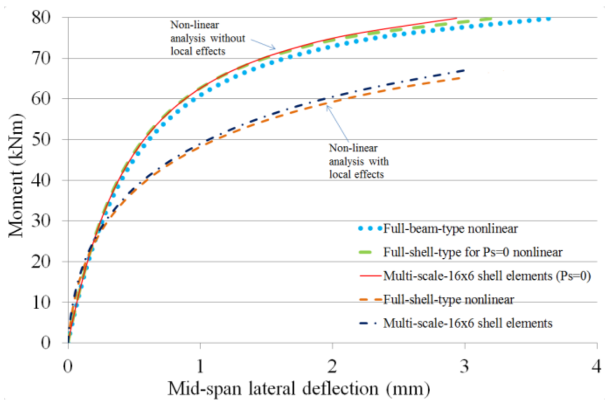

Fig. 12 Load-deflection curve based on different modelling types

The flanges and the web of the beam is composed of 8 layers of glass-epoxy with angle-ply lay-ups of $[0/\text{-}45/90/45]_S$. Similar to the previous example, the beam is analysed using beam, shell and multi-scale models. 8 equal-span elements are used for the beam model while the shell elements have an approximate size of 200 mm × 200 mm. The loading is applied at two stages: firstly, only the global concentrated bending moments are applied and secondly the load couple P_S = 15 kN are introduced to create the localized behaviour. Apart from that, a very small horizontal load (P_B = 0.1 kN) is applied in order to initiate the lateral buckling behaviour in the first analysis. The multi-scale model is created by applying local shell elements in the vicinity of the local load couple (i.e., z = 1400 mm to z = 4600 mm) by using 16 × 6 shell elements, as demonstrated in Fig. 11.

The buckling behaviour is depicted using the lateral deflections of the beam mid-span (Fig. 12). It can be observed that the reduction in the lateral buckling critical load, caused by the softening effect of the localized load couple, is captured accurately by the use of multi-scale method.

6. Conclusions

In this paper, a global-local analysis method based on the Bridging Multiscale Method (BMM) was developed for the analysis of composite thin-walled members. A coarse-scale decomposition operator was proposed based on kinematic arguments, which associates the beam solution as the coarse-scale component of the shell solution. This decomposition allows for the method to incorporate the effects of local deformations on the overall behaviour of the thin-walled member by using a shell model only within the region of local deformations. Thin-walled column and beam buckling cases were then analysed to show that the load carrying capacity can be influenced significantly by the local deformations, and the results of the global-local analysis procedure proposed herein were compared with those produced from full shell and beam-type analyses. In all cases, by selecting a sufficiently wide span of the local shell model in the multi-scale analyses, it was confirmed that the behaviour according to the full shell-type analysis can be captured very accurately by using the global-local analysis technique introduced in the paper.

References

Babuška, I. and Melenk, J.M. (1997), "The partition of unity method", *Int. J. Numer. Method. Eng.*, **40**(4), 727-758.

Babuška, I., Banerjee, U. and Osborn, J.E. (2003), "Survey of meshless and generalized finite element methods: A unified approach", *Acta Numer.*, **12**, 1-125.

Back, S.Y. and Will, K.M. (2008), "Shear-flexible thin-walled element for composite I-beams", *Eng. Struct.*, **30**(5), 1447-1458.

Batoz, J.L. and Tahar, M.B. (1982), "Evaluation of a new quadrilateral thin plate bending element", *Int. J. Numer. Method. Eng.*, **18**(11), 1655-1677.

Bauld, N.R. and Tzeng, L.S. (1984), "A Vlasov theory for fiber-reinforced beams with thin-walled open cross sections", *Int. J. Solid. Struct.*, **20**(3), 277-297.

Belytschko, T., Krongauz, Y., Organ, D., Fleming, M. and Krysl, P. (1996), "Meshless methods: An overview and recent developments", *Comput. Method. Appl. Mech. Eng.*, **139**(1-4), 3-47.

Belytschko, T., Moës, N., Usui, S. and Parimi, C. (2001), "Arbitrary discontinuities in finite elements", *Int. J. Numer. Method. Eng.*, **50**(4), 993-1013.

Bradford, M.A. (1992), "Lateral-distortional buckling of steel I-section members", *J. Construct. Steel Res.*, **23**(1-3), 97-116.

Bradford, M.A. and Hancock, G.J. (1984), "Elastic interaction of local and lateral buckling in beams", *Thin-Wall. Struct.*, **2**(1), 1-25.

Cardoso, J.E.B., Benedito, N.M.B. and Valido, A.J.J. (2009), "Finite element analysis of thin-walled composite laminated beams with geometrically nonlinear behavior including warping deformation", *Thin-Wall. Struct.*, **47**(11), 1363-1372.

Davies, J.M., Leach, P. and Heinz, D. (1994), "Second-order generalised beam theory", *J. Construct. Steel Res.*, **31**(2-3), 221-241.

Erkmen, R.E. (2013), "Bridging multi-scale approach to consider the effects of local deformations in the analysis of thin-walled members", *Computat. Mech.*, **52**(1), 65-79.

Erkmen, E. and Bradford, M.A. (2011), "Coupling of finite element and meshfree methods be for locking-free analysis of shear-deformable beams and plates", *Eng. Computat.*, **28**(8), 1003-1027.

Feyel, F. (2003), "A multilevel finite element method (FE2) to describe the response of highly non-linear structures using generalized continua", *Comput. Method. Appl. Mech. Eng.*, **192**(28-30), 32-44.

Fish, J., Markolefas, S., Guttal, R. and Nayak, P. (1994), "On adaptive multilevel superposition of finite element meshes for linear elastostatics", *Appl. Numer. Math.*, **14**(1-3), 135-164.

Geers, M.G.D., Kouznetsova, V.G. and Brekelmans, W.A.M. (2010), "Multi-scale computational homogenization: Trends and challenges", *J. Computat. Appl. Math.*, **234**(7), 2175-2182.

Hughes, T.J.R. and Sangalli, G. (2007), "Variational multiscale analysis: The fine-scale green's function, projection, optimization, localization, and stabilized methods", *SIAM J. Numer. Anal.*, **45**(2), 539-557.

Hughes, T.J.R., Feijóo, G.R., Mazzei, L. and Quincy, J.B. (1998), "The variational multiscale method - A paradigm for computational mechanics", *Comput. Method. Appl. Mech. Eng.*, **166**(1-2), 3-24.

Ibrahimbegovic, A., Taylor, R.L. and Wilson, E.L. (1990), "Robust quadrilateral membrane finite element with drilling degrees of freedom", *Int. J. Numer. Method. Eng.*, **30**(3), 445-457.

Kadowaki, H. and Liu, W.K. (2004), "Bridging multi-scale method for localization problems", *Comput. Method. Appl. Mech. Eng.*, **193**(30-32), 3267-3302.
Kim, N.I., Shin, D.K. and Kim, M.Y. (2007), "Exact lateral buckling analysis for thin-walled composite beam under end moment", *Eng. Struct.*, **29**(8), 1739-1751.
Kollár, L.P. (1991), "Mechanics of laminated composite plates and shells", *Int. J. Solid. Struct.*, **38**(42), 7525-7541.
Lee, J. (2006), "Lateral buckling analysis of thin-walled laminated composite beams with monosymmetric sections", *Eng. Struct.*, **28**(14), 1997-2009.
Lee, J., Kim, S.E. and Hong, K. (2002), "Lateral buckling of I-section composite beams", Eng. Struct., **24**(7), 955-964.
Li, S. and Liu, W.K. (2002), "Meshfree and particle methods and their applications", *Appl. Mech. Rev.*, **55**(1), 1-34.
Liu, W.K., Li, S. and Belytschko, T. (1997), "Moving least-square reproducing kernel methods (I) methodology and convergence", *Comput. Method. Appl. Mech. Eng.*, **143**(1-2), 113-154.
Liu, W.K., Hao, S., Belytschko, T., Li, S. and Chang, C.T. (2000), "Multi-scale methods", *Int. J. Numer. Method. Eng.*, **47**(7), 1343-1361.
Machado, S.P. (2010), "Interaction of combined loads on the lateral stability of thin-walled composite beams", *Eng. Struct.*, **32**(11), 3516-3527.
Mittelstedt, C. (2007), "Local buckling of wide-flange thin-walled anisotropic composite beams", *Arch. Appl. Mech.*, **77**(7), 439-452.
Oden, J.T., Prudhomme, S., Romkes, A. and Bauman, P.T. (2006), "Multiscale modeling of physical phenomena: Adaptive control of models", *SIAM J. Scientif. Comput.*, **28**(6), 2359-2389.
Omidvar, B. and Ghorbanpoor, A. (1996), "Nonlinear FE solution for thin-walled open-section composite beams", *J. Struct. Eng.*, **122**(11), 1369-1377.
Pandey, M.D., Kabir, M.Z. and Sherbourne, A.N. (1995), "Flexural-torsional stability of thin-walled composite I-section beams", *Compos. Eng.*, **5**(3), 321-342.
Qian, D., Wagner, G.J. and Liu, W.K. (2004), "A multi-scale projection method for the analysis of carbon nanotubes", *Comput. Method. Appl. Mech. Eng. Computat.*, **193**(17-20), 1603-1632.
Reddy, J.N. (2004), *Mechanics of Laminated Composite Plates and Shells: Theory and Analysis*, (2nd Edition), CRC Press, Boca Raton, FL, USA.
Roberts, T.M. (2002), "Influence of shear deformation on buckling of pultruded fiber reinforced plastic profiles", *J. Compos. Construct.*, **6**(4), 241-248.
Roberts, T.M. and Masri, H.M.K.J.A.H. (2003), "Section properties and buckling behavior of pultruded FRP profiles", *J. Reinf. Plast. Compos.*, **22**(14), 1305-1317.
Ronagh, H.R. and Bradford, M.A. (1996), "A rational model for the distortional buckling of tapered members", *Comput. Method. Appl. Mech. Eng.*, **130**(3-4), 263-277.
Sapkás, A. and Kollár, L.P. (2002), "Lateral-torsional buckling of composite beams", *Int. J Solid. Struct.*, **39**(1), 2939-2963.
Schafer, B.W. (2008), "Review: The direct strength method of cold-formed steel member design", *J. Construct. Steel Res.*, **64**(7-8), 766-778.
Strouboulis, T., Copps, K. and Babuška, I. (2001), "Computational mechanics advances. The generalized finite element method", *Comput. Method. Appl. Mech. Eng.*, **190**(32-33), 4081-4193.
Trahair, N.S. (2003), Flexural-Torsional Buckling of Structures, Spon Press, London, UK.
Zienkiewicz, O.C. and Taylor, R.L. (2000), *The Finite Element Method for Solid and Structural Mechanics*, (6th Edition), Butterworth-Heinemann, Oxford, UK.

BU

Appendix A

Strains, displacements and stresses of the beam element

The beam element strain vector can be written in terms of linear and second order nonlinear terms, i.e., $\bar{\boldsymbol{\varepsilon}} = \bar{\boldsymbol{\varepsilon}}_L + \bar{\boldsymbol{\varepsilon}}_N$. The linear axial and shear strains $\bar{\boldsymbol{\varepsilon}}_L$ and $\bar{\gamma}_L$, respectively can be obtained in terms of the displacements $\bar{u}$, $\bar{v}$, $\bar{w}$ and the angle of twist $\bar{\phi}$ (Fig. 1(a)) as

$$\bar{\boldsymbol{\varepsilon}}_L = \langle \bar{\varepsilon}_L \quad 0 \quad \bar{\gamma}_L \quad 0 \rangle^{\mathrm{T}} = \bar{\mathbf{S}} \bar{\boldsymbol{\chi}}_L \tag{A1}$$

which can be decomposed in terms of the matrix of cross-sectional coordinates

$$\bar{\mathbf{S}} = \begin{bmatrix} 1 & -\bar{x} & -\bar{y} & -\bar{\omega} & \bar{x}^2+\bar{y}^2 & 0 \\ 0 & 0 & 0 & 0 & 0 & 0 \\ 0 & 0 & 0 & 0 & 0 & -2\bar{r} \\ 0 & 0 & 0 & 0 & 0 & 0 \end{bmatrix} \tag{A2}$$

and the vector of linear displacement derivatives

$$\bar{\boldsymbol{\chi}}_L^{\mathrm{T}} = \langle \bar{w}' \quad \bar{u}'' \quad \bar{v}'' \quad \bar{\phi}'' \quad 0 \quad \bar{\phi}' \rangle. \tag{A3}$$

In Eq. (A2), $\bar{x}$ and $\bar{y}$ identifies the coordinates of a point on the cross-section, and $\bar{r}$ is the normal distance from the mid-surface (Fig. 1(a)). Sectorial area coordinates are used, i.e., $\bar{\omega} = \int h \mathrm{d}\bar{s}$ in which h is the normal distance to the tangent of the point on the section contour from the arbitrarily located pole with $\bar{x}$ and $\bar{y}$ coordinates (a_x, a_y), i.e., $h = (\bar{x} - a_x)\sin\alpha - (\bar{y} - a_x)\cos\alpha$ (Fig. 1(a)), where α is the angle between the $\bar{x}$ and $\bar{s}$ axes. As shown in Fig. 1(a), $\bar{s}$ axis is the tangent to the mid-surface of the cross-section and directed along the contour line. In Eq. (A3), primes denote the derivative with respect to the axial coordinate z. The nonlinear linear strains can be written as (Trahair 2003)

$$\bar{\boldsymbol{\varepsilon}}_N = \langle \bar{\varepsilon}_N \quad 0 \quad \bar{\gamma}_N \quad 0 \rangle^{\mathrm{T}} = \bar{\mathbf{S}} \bar{\boldsymbol{\chi}}_N, \tag{A4}$$

in which $\bar{\varepsilon}_N$ is the nonlinear axial strain and $\bar{\gamma}_N$ is taken as zero. Similar to linear strains, the nonlinear strain vector in Eq. (A4) can be decomposed using the same matrix of cross-sectional coordinates **S** and a vector of second-order displacement derivatives, i.e.

$$\bar{\boldsymbol{\chi}}_N^{\mathrm{T}} = \langle \tfrac{1}{2}\left(\bar{u}'^2 + \bar{v}'^2\right) - a_x \bar{v}'\bar{\phi}' + a_y \bar{u}'\bar{\phi}' + \tfrac{1}{2}\left(a_x^{\,2} + a_y^{\,2}\right)\bar{\phi}'^2 \quad -\bar{v}'\bar{\phi}' + a_x \bar{\phi}'^2 \quad \bar{u}'\bar{\phi}' + a_y \bar{\phi}'^2 \quad 0 \quad \tfrac{1}{2}\bar{\phi}'^2 \quad 0 \rangle, \tag{A5}$$

The element is developed by using a linear interpolation for $\bar{w}$ and cubic interpolations for $\bar{u}$, $\bar{v}$ and $\bar{\phi}$, i.e., $\bar{\mathbf{u}}_a = \bar{\mathbf{X}}_a \bar{\mathbf{d}}$ in which

$$\bar{\mathbf{u}}_a = \langle \bar{w} \quad \bar{u} \quad \bar{v} \quad \bar{\phi} \rangle^{\mathrm{T}}, \tag{A6}$$

$$\bar{\mathbf{X}}_a = \left[\begin{array}{c:c:c:c} \mathbf{L}^{\mathrm{T}} & \mathbf{0} & \mathbf{0} & \mathbf{0} \\ \hdashline \mathbf{0} & \mathbf{H}^{\mathrm{T}} & \mathbf{0} & \mathbf{0} \\ \hdashline \mathbf{0} & \mathbf{0} & \mathbf{H}^{\mathrm{T}} & \mathbf{0} \\ \hdashline \mathbf{0} & \mathbf{0} & \mathbf{0} & \mathbf{H}^{\mathrm{T}} \end{array}\right], \tag{A7}$$

where

$$\mathbf{L} = \left\langle 1 - \frac{\bar{z}}{L} \quad \frac{\bar{z}}{L} \right\rangle^{\mathrm{T}}, \tag{A8}$$

$$\mathbf{H} = \left\langle 1 - \frac{3\bar{z}^2}{L^2} + \frac{2\bar{z}^3}{L^3} \quad \bar{z} - \frac{2\bar{z}^2}{L} + \frac{\bar{z}^3}{L^2} \quad \frac{3\bar{z}^2}{L^2} - \frac{2\bar{z}^3}{L^3} \quad -\frac{\bar{z}^2}{L} + \frac{\bar{z}^3}{L^2} \right\rangle^{\mathrm{T}}, \tag{A9}$$

The nodal displacement vector $\bar{\mathbf{d}}$ of the beam type finite element can be written as

$$\bar{\mathbf{d}} = \langle \bar{w}_1 \quad \bar{w}_2 \quad \bar{u}_1 \quad \bar{\theta}_{x1} \quad \bar{u}_2 \quad \bar{\theta}_{x2} \quad \bar{v}_1 \quad \bar{\theta}_{y1} \quad \bar{v}_2 \quad \bar{\theta}_{y2} \quad \bar{\phi}_1 \quad \bar{\varphi}_1 \quad \bar{\phi}_2 \quad \bar{\varphi}_2 \rangle^{\mathrm{T}}, \tag{A10}$$

in which subscripts 1 and 2 refer to each of the two end nodes, $\bar{\theta}_x$ and $\bar{\theta}_y$ refer to the bending rotations in $\bar{z}-\bar{x}$ and $\bar{z}-\bar{y}$ planes (Fig. 1(a)) respectively, and $\bar{\varphi}$ is associated with the warping deformations of the cross-section. The displacement vector of a point α on the cross-section can be written as $\bar{\mathbf{u}} = \mathbf{N}\bar{\mathbf{d}}$, where

$$\bar{\mathbf{u}} = \langle \bar{w}_\alpha \quad \bar{u}_\alpha \quad \bar{u}'_\alpha \quad \bar{v}_\alpha \quad \bar{v}'_\alpha \quad \bar{\phi}_\alpha \rangle^{\mathrm{T}} \tag{A11}$$

and $\mathbf{N} = \mathbf{YZ}$ in which

$$\mathbf{Z} = \left[\begin{array}{c:c:c:c} \mathbf{L}^{\mathrm{T}} & \mathbf{0} & \mathbf{0} & \mathbf{0} \\ \hdashline \mathbf{0} & \mathbf{H}^{\mathrm{T}} & \mathbf{0} & \mathbf{0} \\ \hdashline \mathbf{0} & \mathbf{0} & \mathbf{H}^{\mathrm{T}} & \mathbf{0} \\ \hdashline \mathbf{0} & \mathbf{0} & \mathbf{0} & \mathbf{H}^{\mathrm{T}} \\ \hdashline \mathbf{0} & \dfrac{\mathrm{d}\mathbf{H}^{\mathrm{T}}}{\mathrm{d}\bar{z}} & \mathbf{0} & \mathbf{0} \\ \hdashline \mathbf{0} & \mathbf{0} & \dfrac{\mathrm{d}\mathbf{H}^{\mathrm{T}}}{\mathrm{d}\bar{z}} & \mathbf{0} \\ \hdashline \mathbf{0} & \mathbf{0} & \mathbf{0} & \dfrac{\mathrm{d}\mathbf{H}^{\mathrm{T}}}{\mathrm{d}\bar{z}} \end{array}\right], \tag{A12}$$

$$\mathbf{Y}=\begin{bmatrix} 1 & 0 & 0 & 0 & -\bar{x} & -\bar{y} & -\bar{\omega} \\ 0 & 1 & 0 & -\left(\bar{y}-a_y\right) & 0 & 0 & 0 \\ 0 & 0 & 0 & 0 & 1 & 0 & -\left(\bar{y}-a_y\right) \\ 0 & 0 & 1 & \left(\bar{x}-a_x\right) & 0 & 0 & 0 \\ 0 & 0 & 0 & 0 & 0 & -1 & -\left(\bar{x}-a_x\right) \\ 0 & 0 & 0 & -1 & 0 & 0 & 0 \end{bmatrix}. \tag{A13}$$

The matrix $\overline{\mathbf{B}}$ can be written as

$$\overline{\mathbf{B}}=\begin{bmatrix} 1 & \bar{u}'+a_y\bar{\phi}' & 0 & \bar{v}'-a_x\bar{\phi}' & 0 & 0 & a_y\bar{u}'-a_x\bar{v}'+\left(a_x{}^2+a_y{}^2\right)\bar{\phi}' & 0 \\ 0 & 0 & 1 & \bar{\phi} & 0 & 0 & 2a_x\bar{\phi}'+\bar{v}' & 0 \\ 0 & \bar{\phi} & 0 & 0 & 1 & 0 & 2a_y\bar{\phi}'+\bar{u}' & 0 \\ 0 & 0 & 0 & 0 & 0 & 0 & 0 & 1 \\ 0 & 0 & 0 & 0 & 0 & 0 & \bar{\phi}' & 0 \\ 0 & 0 & 0 & 0 & 0 & 0 & 1 & 0 \end{bmatrix}\nabla\overline{\mathbf{X}}_a, \tag{A14}$$

in which

$$\nabla=\begin{bmatrix} \dfrac{\mathrm{d}}{\mathrm{d}z} & 0 & 0 & 0 & 0 & 0 & 0 & 0 \\ 0 & \dfrac{\mathrm{d}}{\mathrm{d}z} & \dfrac{\mathrm{d}^2}{\mathrm{d}z^2} & 0 & 0 & 0 & 0 & 0 \\ 0 & 0 & 0 & \dfrac{\mathrm{d}}{\mathrm{d}z} & \dfrac{\mathrm{d}^2}{\mathrm{d}z^2} & 0 & 0 & 0 \\ 0 & 0 & 0 & 0 & 0 & 1 & \dfrac{\mathrm{d}}{\mathrm{d}z} & \dfrac{\mathrm{d}^2}{\mathrm{d}z^2} \end{bmatrix}^{\mathrm{T}}. \tag{A15}$$

Constitutive relations for the beam element

It is assumed that perfect interlaminar bond exists between the layers. For a laminate composed of *n* orthotropic layers, the orientation of the local $\bar{s}_k\bar{z}_k$ - plane with respect to the global $\bar{s}\bar{z}$ -plane is determined by the angle about the $\bar{r}$ -axis Φ (positive according to the opposite of the right hand rule) between $\bar{z}$ and $\bar{z}_k$ (Fig. 1(b)). For the k^{th} layer, the stress-strain relationship can be written as (Back and Will 2008, Lee 2006, Lee *et al*. 2002)

$$\bar{\boldsymbol{\sigma}}^{(k)} = \begin{Bmatrix} \bar{\sigma}_z^{(k)} \\ 0 \\ \bar{\tau}_{zs}^{(k)} \\ 0 \end{Bmatrix} = \bar{\mathbf{Q}}^{(k)} \bar{\boldsymbol{\varepsilon}}, \tag{A16}$$

where

$$\bar{\mathbf{Q}}^{(k)} = \begin{bmatrix} \bar{Q}_{11}^{*(k)} & 0 & \bar{Q}_{16}^{*(k)} & 0 \\ 0 & 0 & 0 & 0 \\ \bar{Q}_{16}^{*(k)} & 0 & \bar{Q}_{66}^{*(k)} & 0 \\ 0 & 0 & 0 & 0 \end{bmatrix} \tag{A17}$$

in which $\bar{Q}_{11}^{*(k)} = \bar{Q}_{11}^{(k)} - \bar{Q}_{12}^{(k)2} / \bar{Q}_{22}^{(k)}$, $\bar{Q}_{16}^{*(k)} = \bar{Q}_{16}^{(k)} - \bar{Q}_{12}^{(k)} \bar{Q}_{26}^{(k)} / \bar{Q}_{22}^{(k)}$ and $\bar{Q}_{66}^{*(k)} = \bar{Q}_{66}^{(k)} - \bar{Q}_{26}^{(k)2} / \bar{Q}_{22}^{(k)}$ (Back and Will 2008, Lee *et al*. 2002). These coefficients can be found in (Back and Will 2008, Lee 2006, Lee *et al*. 2002, Reddy 2004).

Appendix B

Strains of shell element

The strains of the shell-type element are composed of strains due to plate bending deformations $\hat{\boldsymbol{\varepsilon}}_b$, membrane deformations $\hat{\boldsymbol{\varepsilon}}_m$, and strains due to second order membrane and plate bending action $\hat{\boldsymbol{\varepsilon}}_N$, i.e.

$$\hat{\boldsymbol{\varepsilon}} = \hat{\boldsymbol{\varepsilon}}_b + \hat{\boldsymbol{\varepsilon}}_{mm} + \hat{\boldsymbol{\varepsilon}}_N , \tag{B1}$$

where the plate bending strains can be written as

$$\hat{\boldsymbol{\varepsilon}}_b = -z \left\{ \begin{array}{c} \dfrac{\partial \hat{\theta}_x}{\partial x} \\ \dfrac{\partial \hat{\theta}_y}{\partial y} \\ \dfrac{\partial \hat{\theta}_x}{\partial y} + \dfrac{\partial \hat{\theta}_y}{\partial x} \\ \hline 0 \end{array} \right\} . \tag{B2}$$

The second term in Eq. (B1) can be written as

$$\hat{\boldsymbol{\varepsilon}}_{mm} = \left\{ \begin{array}{c} \dfrac{\partial \hat{u}_0}{\partial x} \\ \dfrac{\partial \hat{v}_0}{\partial y} \\ \dfrac{\partial \hat{u}_0}{\partial y} + \dfrac{\partial \hat{v}_0}{\partial x} \\ \hline \dfrac{1}{2}\left(\dfrac{\partial \hat{v}_0}{\partial x} - \dfrac{\partial \hat{u}_0}{\partial y} \right) - \hat{\phi}_z \end{array} \right\} = \left\{ \begin{array}{c} \hat{\boldsymbol{\varepsilon}}_m \\ \hline \dfrac{1}{2}\left(\dfrac{\partial \hat{v}_0}{\partial x} - \dfrac{\partial \hat{u}_0}{\partial y} \right) - \hat{\phi}_z \end{array} \right\} , \tag{B3}$$

in which $\hat{\boldsymbol{\varepsilon}}_m$ is the vector of membrane strains and the last row in Eq. (B3) contains the skew symmetric part of the membrane strains introduced to avoid numerical stability issues when drilling rotations $\hat{\phi}_z$ are used with Allman-type interpolations (Ibrahimbegovic *et al.* 1990). The non-linear strain component can be written as

$$\hat{\boldsymbol{\varepsilon}}_N = \left\{ \begin{array}{c} \frac{1}{2}\left(\frac{\partial \hat{w}_0}{\partial x}\right)^2 + \frac{1}{2}\left(\frac{\partial v_0}{\partial x}\right)^2 \\ 0 \\ 0 \\ \hdashline 0 \end{array} \right\}. \tag{B4}$$

As the membrane axial strain and shear strain components of the shell can be captured by using the rigid cross-section assumption, the rest of the shell strains are the fine-scale strains in the current formulation, i.e.

$$\boldsymbol{\varepsilon}' = -z \left\{ \begin{array}{c} \frac{\partial \hat{\theta}_x}{\partial x} \\ \frac{\partial \hat{\theta}_y}{\partial y} \\ \frac{\partial \hat{\theta}_x}{\partial y} + \frac{\partial \hat{\theta}_y}{\partial x} \\ \hdashline 0 \end{array} \right\} + \left\{ \begin{array}{c} \frac{1}{2}\left(\frac{\partial \hat{w}_0}{\partial x}\right)^2 + \frac{1}{2}\left(\frac{\partial v_0}{\partial x}\right)^2 \\ 0 \\ 0 \\ \hdashline 0 \end{array} \right\} + \left\{ \begin{array}{c} 0 \\ \frac{\partial \hat{v}_0}{\partial y} \\ 0 \\ \hdashline \frac{1}{2}\left(\frac{\partial \hat{v}_0}{\partial x} - \frac{\partial u_0}{\partial y}\right) - \hat{\phi}_z \end{array} \right\}. \tag{B5}$$

Constitutive relations of the shell element

For a laminate composed of n orthotropic layers, the orientation of the fibre attached $x_k y_k$-axes with respect to the plate's local xy axes is determined by the angle Φ which is the angle about plate's local z-axis (positive according to the right hand rule) between x and x_k (Fig. 2(a)). In that case Φ is the same angle used in Appendix A. Assuming that perfect interlaminar bond exists between the layers, the stress-strain relationship for the k^{th} layer according to the plate local axis directions can be written as (Reddy 2004)

$$\hat{\boldsymbol{\sigma}}^{(k)} = \left\{ \begin{array}{c} \hat{\sigma}_x^{(k)} \\ \hat{\sigma}_y^{(k)} \\ \hat{\tau}_{xy}^{(k)} \\ \hdashline \hat{\tau}_m^{(k)} \end{array} \right\} = \hat{\mathbf{Q}}^{(k)} \boldsymbol{\varepsilon}, \tag{B6}$$

where

$$\hat{\mathbf{Q}}^{(k)} = \left[\begin{array}{ccc|c} \bar{Q}_{11}^{(k)} & \bar{Q}_{12}^{(k)} & \bar{Q}_{16}^{(k)} & 0 \\ \bar{Q}_{12}^{(k)} & \bar{Q}_{22}^{(k)} & \bar{Q}_{26}^{(k)} & 0 \\ \bar{Q}_{16}^{(k)} & \bar{Q}_{26}^{(k)} & \bar{Q}_{66}^{(k)} & 0 \\ \hline 0 & 0 & 0 & \bar{Q}_{66}^{(k)} \end{array}\right], \tag{B7}$$

in which the coefficients are as given in (Back and Will 2008, Lee 2006, Lee *et al*. 2002, Reddy 2004). It should be noted that the last diagonal term in Eq. (B7) is because of the modification introduced into the potential energy functional.